

Modelling of Surface PM Machine Using Soft Magnetic Composites and a Bonded Magnet Ring

Chun Tang, Wen L. Soong, Gene S. Liew and Nesimi Ertugrul

Abstract -- This paper examines the modelling of a 1.6 kW, 3,000 rpm surface permanent magnet machine which was constructed using soft magnetic composites (SMC) stator tooth segments and a bonded rare-earth magnet ring. It was designed for high torque density and efficiency, and low cogging torque.

Both 2D and 3D finite-element model results are provided and compared to the experimental measurements of the flux densities, back-EMF, cogging torque, inductance and power losses. Challenges were found in modelling the magnetization of the bonded-ring magnet. The rated efficiency and field-weakening performance are examined by using both measured and finite-element calculated parameters.

Index Terms-- Permanent magnet machines, segmented stators, soft magnetic composites, finite-element analysis, bonded magnets.

I. INTRODUCTION

SOFT magnetic composites (SMC), consisting of insulated iron powder moulded under high pressure in a die, offers intriguing opportunities for the stator cores of electrical machines due to its simplicity of manufacturing and the flexibility in being able to cater for various three-dimensional (3D) design geometries [1-3]. However some challenges with SMC include higher iron losses, lower permeability and a lower saturation flux density than conventional lamination materials [6].

SMC is well suited to a segmented tooth stator construction where the simple concentrated stator coils can be wound around the teeth before assembly, allowing potentially higher packing factors. The 3D flux capability of SMC can also be used with the axial length of the stator tooth tips and yoke being extended beyond that of the stator tooth body such that the stator end-windings are enclosed within the stator core [4-5]. The increased magnetic stack length should enable a higher torque density.

Surface permanent magnet (PM) machines often use sintered rare-earth magnets to obtain the highest airgap flux densities and hence torque density. However concentrated windings produce non-sinusoidal stator mmf waveforms which can produce high eddy-current losses in the conductive sintered rotor magnets. These losses can be reduced by segmenting the rotor magnets or by using bonded magnets which have higher resistivity. When using bonded magnets, the magnets can be constructed as a full ring and then magnetised. This provides a simpler rotor construction which avoids the need to assemble the individual magnet segments.

The 1.6kW, 3,000 rpm, 12-slot, 10-pole surface PM SMC machine constructed in this paper was designed by the authors in an earlier paper [7] with the aim of achieving high efficiency, low cogging torque and high torque density. Table 1 gives some key machine design information.

TABLE I. KEY DESIGN INFORMATION OF THE SMC MACHINE

Number of slots	12
Number of poles	10
Stator core	SMC-Somaloy 550 K
- Outer diameter	134 mm
- Stack length	50 mm
Airgap length	1.41 mm
Rotor magnet	Bonded NdFeB ring
- Remanent flux density, B_R	0.71 T
- Relative permeability, μ_r	1.88
- Resistivity,	$2.0 \times 10^{-5} \Omega\text{m}$
Rotor back-iron (solid)	
- Resistivity,	$2.22 \times 10^{-7} \Omega\text{m}$

This paper continues with this optimized SMC model, discussing the finite-element modelling, prototype construction, experimental parameter measurement and performance predictions.

II. 2D/3D FINITE-ELEMENT MODELING

The majority of electric machines use laminations which have two-dimensional (2D) flux distributions and hence 2D finite-element (FE) analysis is commonly used for their analysis. Some machine geometries inherently have 3D flux distributions, these are often constructed using SMC and require 3D FE analysis. Examples are: claw-pole transverse flux machines [8-9] and axial-field machines [10]. Challenges with 3D versus 2D FE analysis include longer model development, longer solution times and difficulties in visualizing the simulation results.

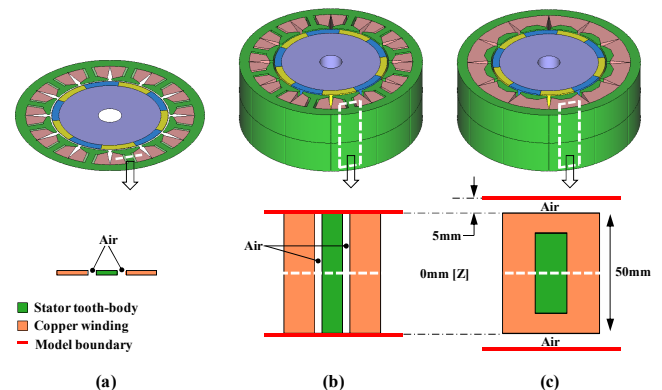


Figure 1: The equivalent 2D (a), simplified 3D extrusion (b) and full 3D model (c).

The proposed SMC machine design is based on an extruded 2D cross-section, has a pseudo-3D design feature

This work was supported by the Australian Research Council projects LP0455574 and DP0988255.

C. Tang, W.L. Soong and N. Ertugrul are with the University of Adelaide, SA 5005, Australia. (e-mail: ctang@eleceng.adelaide.edu.au).

G.S. Liew is with SAGE Automation, 34 Bennet Avenue, Melrose Park, SA 5039, Australia.

where the axial length of the tooth body is shorter than that of the tooth tips and stack length. This section discusses three FE models for the machine, one 2D and two 3D models. The model predictions will be compared against one another and with experimental results in later sections of this paper.

A. The Three Finite-Element Models

Firstly an equivalent 2D FE model (2DEqu) was considered. The shorter axial length of the tooth body compared to the tooth tips and stator yoke was modelled by reducing the tooth width to an “equivalent” value which gives the same tooth body cross-section area as the actual machine [5]. This is shown in Figure 1a. The gap between the winding and the now narrower tooth body is modelled as air. Symmetry was used to allow modeling only half the machine cross-section.

Secondly, the 2D model was extruded axially to form a simplified 3D model (2Dext, see Fig. 1b) which has no geometry or material changes in the axial direction and thus should have identical results to the 2D model. The axial symmetry of the machine means only half of it (25mm axial length) needed to be modelled, also no external air region was used. A total of 10 axial layers were used.

The full 3D model (Ext3D, see Fig. 1c) is another extruded model which also uses the same mesh as the 2D model but includes: the shorter axial length of the stator tooth body compared to the stator yoke; the stator end-windings; and a 5mm air region at the edge of the machine. This model closely resembles the actual machine except that the shape of the end-windings is approximated due to the use of an extruded model. No significant changes were found when increasing the end air region beyond 5 mm. A non-extruded 3D model was not used due to the considerably longer model creation and meshing times.

Table II summarizes the mesh information and execution time for the three FE models. The automatic mesh generator was used with the default element sizes shown. Note the model size and execution time increase by about two orders of magnitude between the 2D and 3D models.

TABLE II. MESH INFORMATION AND EXECUTION TIME FOR FEM MODELS

	2DEqu	2DExt	Ext3D
Number of elements	5,100	490,000	290,000
Number of nodes	3,500	170,000	85,000
Cross-section element size	2.5mm ²	2.5mm ²	2.5mm ²
Axial element length	-	2.5mm	2.5mm
End air thickness	-	-	5mm
Execution time for 1 elec. cycle (181 steps)	1-2mins	11-13hrs	7-8hrs

Note: Based on using JMAG[®] Studio 10 on a computer with Intel Xeon 2.67GHz CPU.

The prototype machine used a type of SMC known as Somaloy 550 Kenolube (or S550K). The typical B-H characteristic of the S550K SMC material is shown in Figure 2 compared to the commonly used steel, M-19 [11]. The unsaturated permeability of S550K is about 720, which is much lower than the 6,400 for M-19 steel. Besides, the S550K starts saturating from about 0.7 T which is much lower than the 1.5 T for M-19. The SMC machine has a maximum flux density of about 1.5 T. Note that the B-H characteristics of SMC are sensitive to the compaction

process and so vary depending on the exact moulding process.

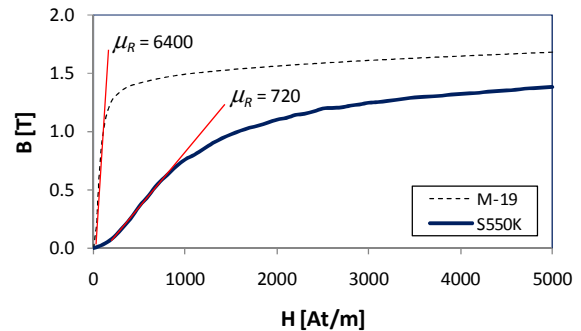


Figure 2: The B-H curve of SMC (S550K) and standard lamination material (M-19)

The rotor magnets and rotor back-iron were modelled as conductors with the resistivity values given in Table I. The simulations modelled the eddy-current effects in the rotor.

III. PROTOTYPE MACHINE CONSTRUCTION

The general approach used for producing prototype SMC machines is by machining the teeth from solid blocks of SMC. However in this prototype the stator teeth were die-cast to give the best dimensional tolerances and surface finish.

With the double-layer, concentrated winding configuration used, every stator tooth segment is wound individually before being assembled together. This should allow a high copper slot fill to be achieved. In practice, only a modest copper packing factor of 30% (area of copper divided by the total slot area) was obtained in the prototype, though later tests showed that with greater care, a value of 40% was achievable. The achievable packing factor was partially limited because the stator tooth geometry used was basically an extruded 2D shape. This meant that the shape of the coil cross-sectional area changed significantly between the slot and the end-winding regions which caused difficulties in producing a compact winding.

The rated stator current was estimated at about 19A, assuming a maximum allowable current density of 10A/mm².

The rotor consists of a bonded rare-earth magnet ring with a solid magnetic back-iron. Figure 3 shows the stator assembly with the rotor magnets and a plastic spacer in the airgap. Figure 4 shows the test-rig used for the experimental testing and the assembled prototype motor.

In the construction method used for motor, the rotor is overhung and supported by two bearings on one side. This resulted in the possibility of significant eccentricity.

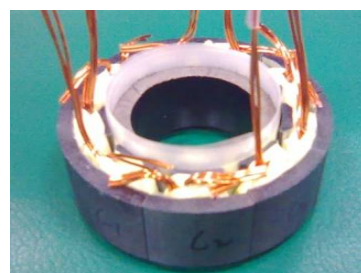


Figure 3: The stator and rotor of the prototype machine

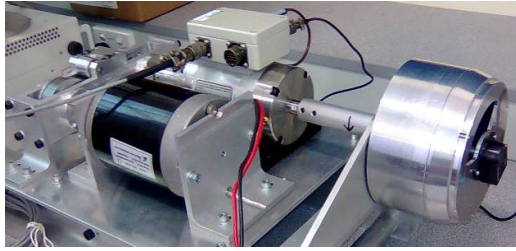


Figure 4: The test rig showing the DC load machine, belt drive, torque transducer and prototype SMC machine (right)

IV. ROTOR MAGNETIZATION INVESTIGATION

The bonded NdFeB magnets can be fabricated by either injection moulding or compression, which allows a wide flexibility in shapes, such as producing a full magnet ring. The use of a plastic binder in the bonded magnets results in a lower remanent flux density but higher resistivity than sintered magnets. The latter is useful to reduce the magnet eddy-current loss in concentrated winding designs [12].

When earlier work has described the use of bonded magnets, these have generally been individual magnet segments [12]. There has been limited work on examining bonded magnet rings [14-17]. The main advantage of using a bonded magnet ring is the simpler motor assembly process.

This section describes the issues found in modelling the magnetization of the custom-made bonded magnet ring. The manufacturer of the ring provided magnetic properties for the magnet material which was shown in Table I. In the absence of any detailed information on the ring's magnetization pattern, it was assumed to be parallel magnetized with a 180° pole-arc and having the remanent flux density and recoil permeability as specified by the manufacturer in Table I.

A. Calculated and Measured Back-EMF

Figure 5 shows the measured and the three FEM calculated line back-EMF waveforms at 3,000rpm.

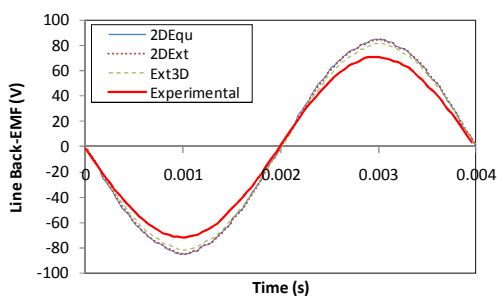


Figure 5: Line back-EMF waveforms at 3,000rpm, comparison of the experimental and the three FE model predictions

The three FE models give similar back-EMF predictions. As expected, the results from the equivalent 2D and simplified 3D extruded models are nearly identical. The full 3D model has a slightly lower back-emf, likely due to the more accurate modelling of localized saturation in the stator yoke due to the shorter axial length of the stator teeth.

The measured back-emf was about 19% below the FE model results. After checking that the dimensions of the machine were accurate, it was thought that this discrepancy is likely due to errors in the assumptions about the modelling of the rotor magnetization. This was investigated as follows.

Firstly, the pole-arc of the rotor magnet poles was checked using a magnetic field viewer consisting a sheet of plastic with iron powder embedded in it. This indicated a magnetic pole arc of about 140° electrical. However, simulations indicated this would only reduce the back-emf by about 4%.

In a second test, the airgap flux density between the rotor ring magnet and a stator pole-piece was measured using a Gauss meter. Due to the thickness of the magnetic field probe, the airgap between the magnet ring and the pole-pieces had to be increased to 2 mm. Based on the measured airgap flux density and a simple magnetic circuit model, it was estimated that the effective magnet remanent flux density was 0.58T which 18% less than the 0.71T given by the manufacturer. Using this value of magnet flux density in the simulations gave a close match between the simulated and experimental back-emf results.

B. Rotor Magnetization Field Shape Testing

In this test, the ring-shaped bonded rotor magnet was placed in free air, and its flux density distribution was measured using a handheld Gauss meter. The variation of the radially-oriented flux density of the magnet was plotted as a function of spatial angle at both the inside and outside surfaces of the ring (see Figure 6) at a mid-axial position.

It was found that the peak flux density on the inside of the ring was about an order of magnitude lower than that on the outside of the ring. These results are considerably different than would be expected from a parallel magnetised rotor where the peak values on the inside and outside of the rotor ring are comparable. They are in fact much closer to the field distribution from a Halbach array [14-17] (see Figures 6 and 7) which is a surprising result. It is estimated that such a magnetic field pattern may be obtained by placing a solid (non-laminated) rotor inside the magnet during the magnetization process.

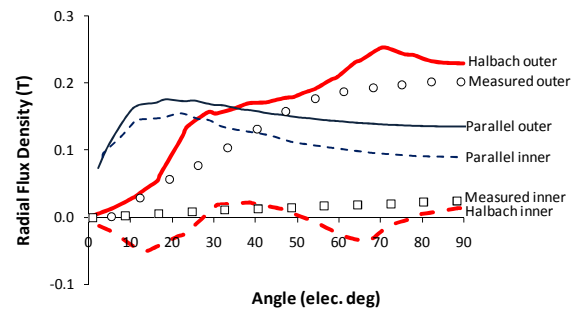


Figure 6: Measured flux density on the surface of bonded-ring magnet in comparison to the FE Halbach 4 segments/pole and parallel magnetization using magnet properties from the manufacturer

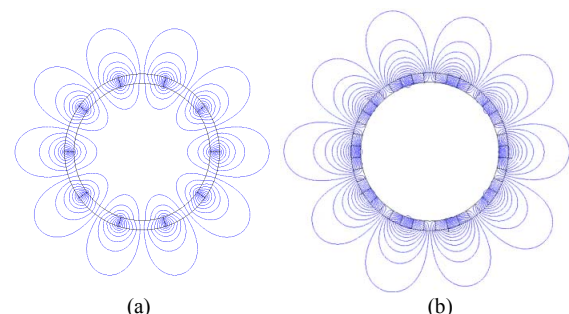


Figure 7: FE flux plots for magnet ring in free air showing two different magnetization patterns: parallel magnetization (a) and a Halbach arrangement with 4 segments/pole (b)

Though the external magnetic field magnitude and distribution is significantly different between the two cases in Figure 7, they become more similar when a rotor back-iron is used for the parallel magnetized case.

V. MACHINE PARAMETERS AND CHARACTERISTICS

The SMC machine characteristics are studied by using the three FE models and verified by experiments. The FE models use the original assumptions about the rotor magnetization.

A. Airgap Flux Density

The calculated rms (averaged circumferentially) airgap flux density produced by the bonded magnet ring under open-circuit conditions was obtained at the mean airgap radius for the 3D model (Ext3D). This was plotted in Figure 8 as a function of the axial position, where 0 mm refers to the middle of the machine and 25 mm to the edge of the stack length. This shows that the airgap field pattern has 3D features within a few mm of the ends of the machine.

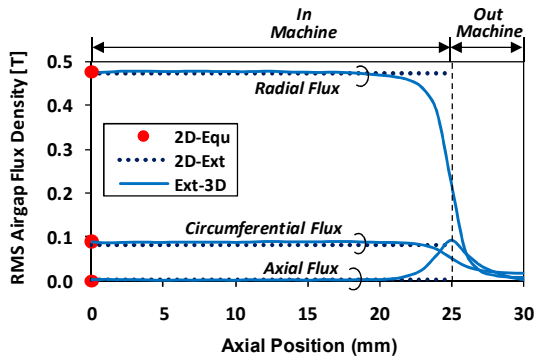


Figure 8: FEM airgap flux densities under open-circuit conditions

B. Tooth and Yoke Flux Density

Figure 9 shows the FE tooth and yoke flux densities as a function of rotor position under open-circuit conditions. For the 3D models, the result shown is averaged axially along the machine. The calculated tooth flux density waveforms are comparable for all three models but there are substantial differences in the yoke flux density waveform. This is likely to be due to the non-uniform flux density distribution in the 3D models.

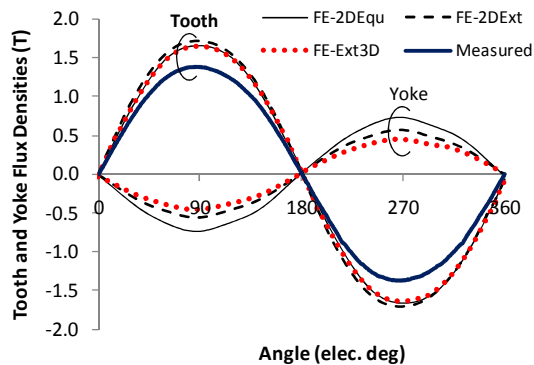


Figure 9: Comparison of FEM and measured tooth and yoke flux density

Figure 9 also shows the measured tooth flux density waveform. This was obtained by integrating the output

voltage of a search coil. As consistent with the back-EMF results seen earlier in Figure 5, the measured tooth flux density is also about 19% lower than the FE results.

C. Open-Circuit Losses

The bearing and windage losses were measured by spinning the rotor in the housing without the stator. After the stator was inserted, the total loss was measured. Then, the stator and rotor losses were obtained by subtracting the bearing and windage losses from the total loss.

A comparison of the open-circuit loss between the 2D FE model (using the 2DEqu model) and the measurements is shown in Figure 10. The measured stator and rotor losses match the FE results well though this needs to be considered in the light of the 19% error in the back-emf results in Figure 5. The SMC material (S550K) used has approximately twice the stator and rotor losses in comparison to conventional lamination (M-19) steel. The bearing and windage losses account for about 1/3 of the total open-circuit loss. The measured open-circuit stator and rotor iron losses at 3,000 rpm correspond to about 5% of rated output power.

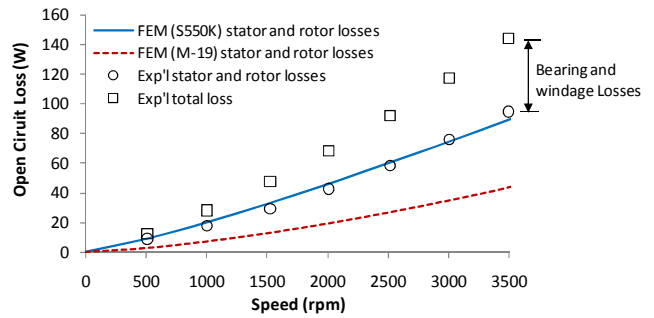


Figure 10: FE and measured open-circuit loss as a function of speed.

D. Flux-Linkage Saturation Characteristics

The machine d - and q -axis flux-linkage versus current curves were measured under static conditions by aligning the rotor appropriately, locking it into position and applying a single-phase mains frequency voltage to the windings [18]. The total instantaneous flux-linkage is calculated by integrating the induced voltage which is obtained by subtracting the resistive voltage drop from the measured terminal voltage. The zero-current d -axis flux linkage is obtained from the open-circuit back-EMF test. The results are shown in Figure 11 for the stator without rotor, and in Figure 12 for the complete motor, and compared to the FE predictions.

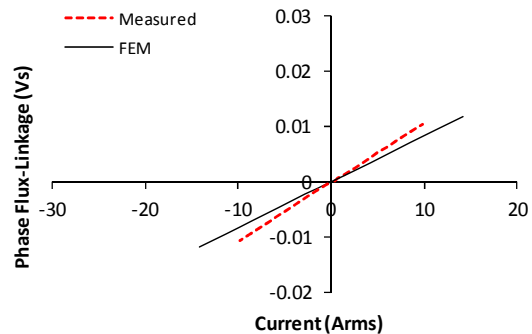


Figure 11: The FE and measured flux-linkage versus current for the case without the rotor in the machine

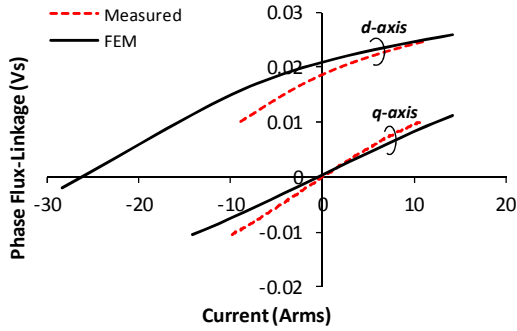


Figure 12: The FE and measured flux-linkage versus d - and q -axis current for the case with the rotor in the machine

The d -axis results show significant saturation for positive values of stator d -axis current (pro-magnetising) whilst negative values of stator d -axis current (de-magnetising) show a far more linear (unsaturated) characteristic. There is little saturation found for the q -axis case and the case without a rotor. The slopes (that is, inductances) of the q -axis and d -axis curves are comparable under unsaturated conditions.

The experimental results show inductance values which are approximately 25% larger than the full 3D model predictions. The reason for this discrepancy is still being investigated.

The characteristic current is the negative d -axis current which is required to reduce the d -axis flux-linkage to zero. The experimental results show a higher inductance and lower back-emf than the measured results. This causes the characteristic current to reduce from the FE estimate of 26A down to about 18A.

Figure 13 shows the FE calculated breakdown of the inductance into magnetizing, slot-leakage and end-leakage components for the q -axis and no rotor cases. This breakdown was obtained using the energy method for calculating inductances. The energy in the airgap and rotor was classified as associated with magnetizing inductance, that in the stator slots (including the end-turns for the Ext3D model) as slot-leakage, and that in the axial air regions in the model as end-leakage.

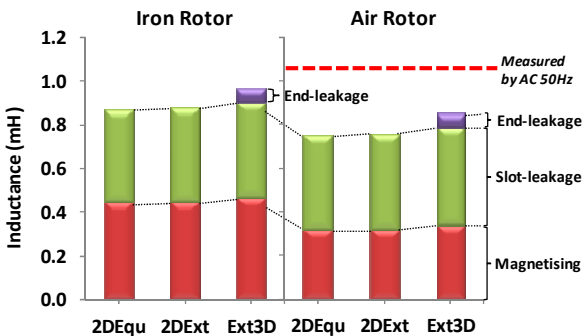


Figure 13: The calculated inductance breakdown for the cases: without magnet (iron rotor) and without magnet or rotor iron (air rotor)

The equivalent 2D model (2DEqu) and simplified 2D model (2DExt) give comparable results as expected. The full 3D model including the end turns (Ext3D) shows comparable slot leakage inductance to the other models. This indicates that the exaggerated stator slot length in the first two models is a good first-order approximation to the inductance of the end-turns in the Ext3D model. The Ext3D model also shows a small amount of end-leakage inductance.

E. Cogging and Ripple Torque

The ratio of the cogging torque to the mechanical rotation frequency is given by the lowest common multiple of the number of slots and poles. For a 12-slot, 10-pole machine this is 60. The cogging torque is sensitive to eccentricity. Figure 14 shows 2D FE cogging torque predictions for an ideal (healthy) machine showing the 60 cogging torque cycles per mechanical revolution, and also the effect of 17% static eccentricity which produces a subharmonic cogging torque frequency at about 11 times per revolution. Note that the prototype machine is prone to eccentricity due to its overhung rotor construction.

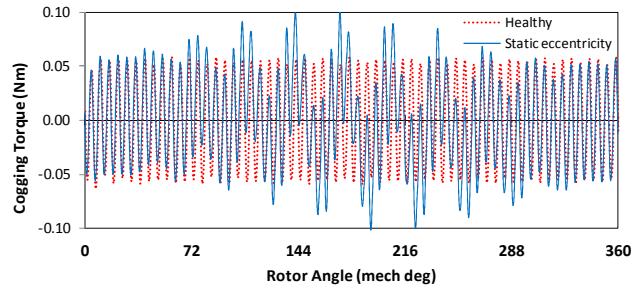


Figure 14: FEM cogging torque with 0% (healthy) and 17% static eccentricity (2DEqu model)

The cogging torque (and back-emf) was measured at 100 rpm and the results shown in Fig. 15 for one mechanical revolution (upper curve) and one electrical revolution (lower curve, also shows FE model predictions). The three FE model predictions are comparable. The cogging torque is small, only a few percent of the rated torque (5 Nm). The measured cogging torque waveforms interestingly show frequencies of about 20 and 40 cycles per revolution. Apart from eccentricity, another possible cause of errors in the prediction of the cogging torque waveform is due to the assembly tolerances of the segmented stator producing a non-uniform stator teeth distribution.

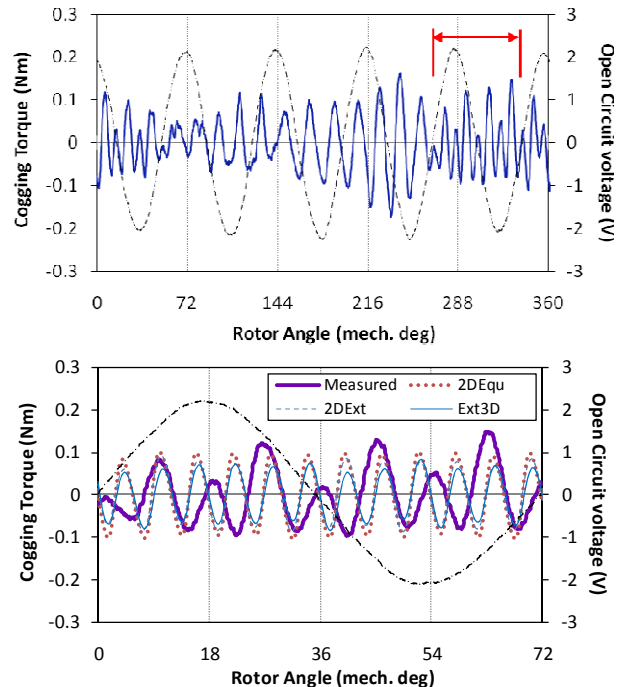


Figure 15: Cogging torque and back-emf versus position for one mechanical revolution (upper) and one electric cycle (lower) at 100rpm. The upper graph shows the measured cogging torque.

VI. MACHINE PERFORMANCE PREDICTIONS

This section investigates the predicted SMC machine performance in terms of the efficiency, power losses and field-weakening characteristics.

A. Calculated Efficiency Map

Figure 16 shows the calculated efficiency map based on the actual copper packing factor of 0.3 and the measured back-emf, stator resistance and open-circuit loss (including bearing losses). The calculated efficiency curves using the FE predicted back-emf is also shown in dashed lines which has an approximately 1% higher efficiency. In producing the efficiency map, it was assumed that the current is in phase with the back-EMF voltage and that the iron loss is only a function of speed and not current.

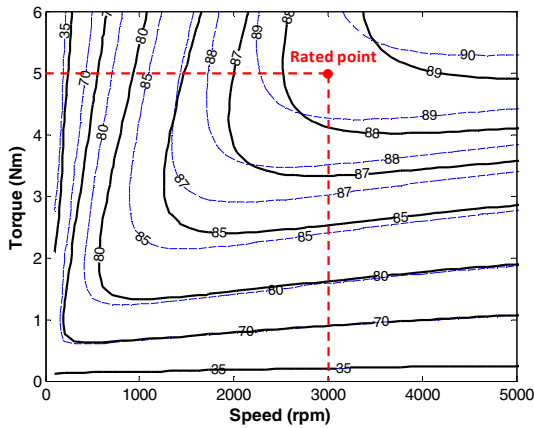


Figure 16: Calculated efficiency map plotted with the measured (solid lines) and FE (dashed lines) back-EMF assuming E and I are in phase

At the rated output of 5 Nm, 3,000 rpm, the machine efficiency is about 88.5% (using the measured back-emf). It is calculated that this would increase to 89.6% if the copper packing factor was increased to 0.4 or 90.7% if the significant bearing losses was reduced to zero, or 91.9% if both were to occur (see Table III).

TABLE III. CALCULATED RATED EFFICIENCY

	With bearing loss	Without bearing loss
0.3 copper packing factor	88.5%	90.7%
0.4 copper packing factor	89.6%	91.9%

B. Calculated Loss Breakdown at Rated Conditions

The calculated loss breakdown for the open-circuit and rated conditions at 3,000 rpm are shown in Figure 17 for each of the three FE models. The losses are broken down into stator yoke, stator teeth (body), stator teeth tip, rotor iron (eddy-current loss in solid back-iron) and magnet eddy-current losses.

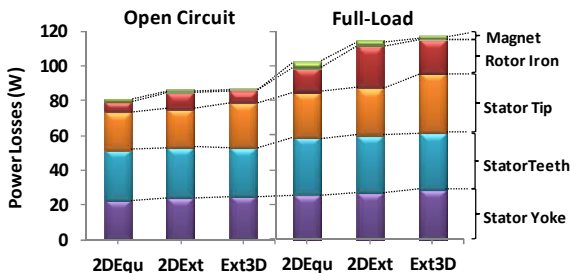


Figure 17: Calculated loss breakdown for open circuit and full-load (5Nm) at 3000rpm: copper loss is not shown

The equivalent 2D model (2DEqu) and simplified 3D model (2DExt) models should have nearly identical results. One key area of difference is that the rotor iron (actually eddy-current) losses nearly doubled in the simplified 3D case. This is likely to be due to this model including the finite axial length effect on the rotor eddy-current distribution which is not included in the equivalent 2D model.

The full 3D model (Ext3D), which includes the end-windings, has a similar total loss prediction to the simplified 3D model (2DExt), however there is a significant difference in the split between the stator tooth tip losses and the rotor iron losses.

The magnitude of the stator copper loss (not shown in Fig. 17) is roughly the same as the total stator iron loss under full-load conditions.

Comparing the open-circuit and full-load losses, the largest increase is in the rotor iron losses followed by the stator tooth tip losses.

C. Effect of I_d/I_q Variations at Rated Speed

To understand the effect of changing the d -axis (I_d) and q -axis (I_q) currents on the various loss components, Fig. 18 shows contour plots of loss as a function of I_q and I_d at 3,000 rpm. These plots were obtained by running simulations with current magnitudes from 1A to 12A with an increment of 1A, while sweeping the current angle (between the back-emf and current) from 0° to 90° with an increment of 5° to obtain a total of 228 simulation points. Note in Figure 18 that the values of I_d shown are negative, that is, they correspond to the demagnetizing condition.

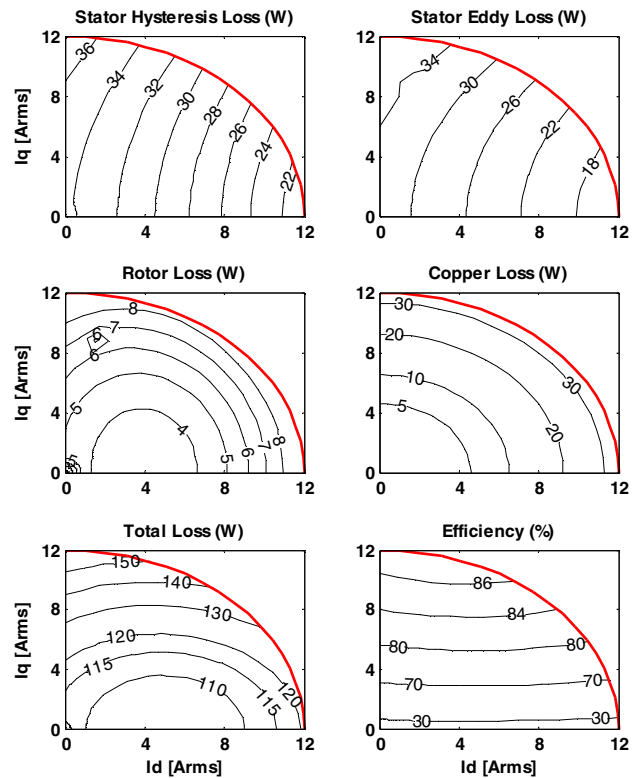


Figure 18: FE calculated power losses and efficiency as a function of I_d and I_q at 3,000 rpm

Figure 18 shows that the stator hysteresis and eddy-current losses are comparable and vary in a similar fashion, generally reducing with increasing (negative) I_d .

The rotor loss, including the magnet and rotor eddy-current loss, forms only a small part in the total loss. It has a minimum value when $I_d = -4A$ at this speed.

The copper loss is proportional to the square of the stator current amplitude. With an input current of 12A, the copper is about half of the total stator iron loss at 3,000 rpm.

The minimum total loss at this speed occurs with a d -axis current of roughly $-6A$. The total loss generally increases with the q -axis current.

Despite the increase of total loss with I_q , the efficiency also rises with I_q due to the increased output power. The efficiency stays roughly constant as the (negative) d -axis current increases from zero as the reduction in iron losses is largely compensated by an increase in the stator copper loss.

D. Calculated Field-Weakening Performance

The calculated machine field-weakening performance is shown in Figure 19, based on a rated current of 18Arms and a rated voltage of 36V. Curves are shown using the measured parameters (solid line) and FE parameters using the Ext3D model (dotted line). Though the rated current 18A used is less than the calculated characteristic current (about 26A), the SMC machine still gives a wide calculated field-weakening performance.

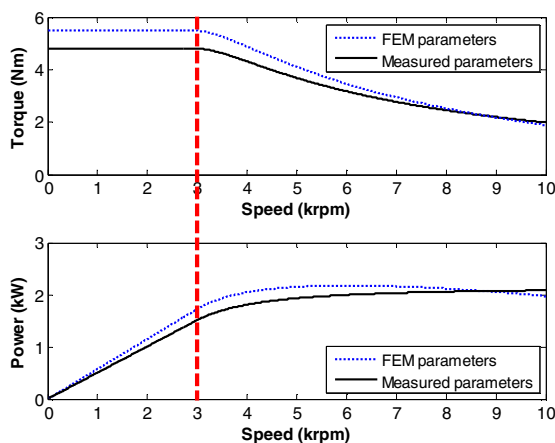


Figure 19: Calculated torque and power versus speed showing the field weakening performance for the SMC machine.

VII. CONCLUSIONS

This paper discussed the finite-element (FE) modelling, experimental verification and performance prediction for an optimized soft magnetic composite (SMC) segmented surface PM machine using a custom bonded ring-shaped rotor magnet. The machine was designed for high torque density and efficiency, and low cogging torque.

With regards to the FE modelling of the proposed machine geometry, an equivalent 2D FE model in which the tooth width was artificially reduced to give the same total tooth body area as the real machine was compared to a more sophisticated extruded 3D model which approximated the end windings. It was found that the 2D FE model gave comparable predictions for back-emf, but slightly lower predictions for the inductances and total iron and magnet losses.

The bonded magnet ring was modelled as being parallel magnetised, 180° pole pitch and with the remanent flux density and recoil permeability as specified by the

manufacturer. This resulted in the measured back-EMF being 19% lower than the FE predictions. Tests indicated firstly that the magnet ring is likely better modelled as a Halbach array, and secondly that the magnet remanent flux density of the ring may be lower than the data sheet value.

Other predicted versus measured parameters which were compared include: open-circuit iron losses, these showed a good correspondence with the calculated values; inductance, the measured results were about 25% higher than the 3D FE results; and cogging torque, where the calculated and measured cogging torque magnitudes were comparable but the actual cogging torque waveform had a significantly lower frequency than expected.

Based on the measured machine parameters, the calculated efficiency of the SMC machine is 88.5% at its rated operating point of 5Nm and 3000rpm. It has a wide calculated field-weakening operating region.

This paper has discussed some of the challenges involved in accurately predicting the performance of the SMC prototype machine and shown there is significant scope for future work to improve the modeling accuracy.

VIII. ACKNOWLEDGMENT

This research was supported by the Australian Research Council (ARC Projects: LP0455574 and DP0988255). The authors would like to thank D. Gehlert and the staff of Intelligent Electric Motor Solutions Pty. Ltd. for manufacturing the machine components and the School of Electrical and Electronic Engineering workshop for constructing the test rig.

IX. REFERENCES

- [1] J. Cros, P. Viarouge, and M. T. Kakhki, "Design and Optimization of Soft Magnetic Composite Machines with Finite Element Methods," *IEEE Trans. Magn.*, vol. 47, pp. 4384-4390, Oct. 2011.
- [2] L. Hultman and A. G. Jack, "Soft Magnetic Composites-Motor Design Issues and Application," in *Proc. Powder Metallurgy and Particulate Materials (PM2TEC)*, Chicago, 2004.
- [3] F. Margnenti, V. D. Colli, R. D. Stefano and A. Cavagninog, "Design Issues of A Fractional-Slot Windings Axial Flux PM Machine With Soft Magnetic Compound Stator," in *Proc. IEEE 33rd Annual Conf. of the Industrial Electronics Society (IECON)*, Taipei, Nov. 2007.
- [4] N. Bianchi, S. Bolognani, and P. Frare, "Design Criteria for High-Efficiency SPM Synchronous Motors," *IEEE Trans. Energy Convers.*, vol. 21, pp. 396-404, Jun. 2006.
- [5] G. S. Liew, E.C.Y. Tsang, N. Ertugrul, W.L. Soong, D. Atkinson and D.B. Gehlert, "Analysis of a Segmented Brushless PM Machine Utilising Soft Magnetic Composites," in *Proc. IEEE 33rd Annual Conf. of the Industrial Electronics Society (IECON)*, Taipei, Nov. 2007.
- [6] A. G. Jack, B.C. Mecrow and P.G. Dickinson, "Iron Loss in Machines with Powdered Iron Stators," in *Proc. IEEE Int. Conf. on Electric Machines and Drives (IEMDC)*, May, 1999, pp. 48-50.
- [7] G. S. Liew, C. Tang, W. L. Soong, N. Ertugrul and D.B. Gehlert, "Finite-Element Analysis and Design of a Radial-Field Brushless PM Machine Utilizing Soft Magnetic Composites," in *Proc. IEEE Int. Conf. on Electric Machines and Drives (IEMDC)*, May, 2011, pp. 930-935.
- [8] Y.G. Guo, J.G. Zhu, Z.W. Lin and J.J. Zhong, "Measurement and modeling of core losses of soft magnetic composites under 3-D magnetic excitations in rotating motors," *IEEE Trans. Magn.* vol.41, no.10, pp. 3925- 3927, Oct. 2005
- [9] J. Cros, P. Viarouge and M.T. Kakhki, "Design and Optimization of Soft Magnetic Composite Machines with Finite Element Methods," *IEEE Trans. Magn.* vol.47, no.10, pp.4384-4390, Oct. 2011
- [10] F. Marignetti, G. Tomassi and P. Cancelliere etc., "Electromagnetic and Mechanical design of a Fractional-slot-windings Axial-flux PM synchronous machine with Soft Magnetic Compound Stator," in *Rec. of IEEE Industry Applications Conf.*, vol.1, pp.62-69, Oct. 2006

- [11] M-19 steel datasheet, available at www.protolam.com/page7.html, accessed on Feb. 10, 2012.
- [12] A.M. El-Refaie, T.M. Jahns, P.J. McCleer and J.W. McKeever, "Experimental verification of optimal flux weakening in surface PM Machines using concentrated windings," *IEEE Trans. Ind. Appl.*, vol.42, no.2, pp. 443-453, Mar. 2006
- [13] Magnets information, available at http://www.mmcmagnetics.com/ourproducts/main_NdFeB.htm#sintered
- [14] Z. Q. Zhu, Z. P. Xia, Y. F. Shi, D. Howe, A. Pride and X. J. Chen, "Performance of Halbach Magnetized Brushless AC Motors", *IEEE Trans. Magn.*, vol. 39, pp. 2992-2994, Sep. 2003.
- [15] K. Halbach, "Design of Permanent Magnet Multipole Magnets with Oriented Rare Earth Cobalt Material," *Nucl. Instrum Method*, vol. 169, pp.1-10, 1980.
- [16] Z. Q. Zhu, Z. P. Xia and D. Howe, "Comparison of Halbach Magnetized Brushless machines having discrete magnet segments or single ring magnet," *IEEE Trans. Magn.*, vol. 38, pp. 2997-2999, 2002.
- [17] Z. Q. Zhu, Z. P. Xia, K. Atallah, G. W. Jewell and D. Howe, "Powder Alignment System for Anisotropic Bonded NdFeB Halbach Cylinders," *IEEE Trans. Magn.*, vol. 36, pp. 3349-3352, 2000.
- [18] W.L. Soong, "Inductance Measurements for Synchronous Machines," PEBN #2, May 2008. Available from <http://www.eleceng.adelaide.edu.au/research/power/pebn/>

X. BIOGRAPHIES

Chun Tang received the B.Eng. degree from the Hefei University of Technology, China, in 2004, and the M.Sc. degree from the University of Adelaide, Australia, in 2010. He is currently working towards the Ph.D. degree in the University of Adelaide. His research interests include

permanent magnet machines, power electronic converters and control, and maximum power extraction control strategies for wind generation systems.

Wen L. Soong (S'89–M'93) was born in Kuala Lumpur, Malaysia. He received the B.Eng. degree from the University of Adelaide, Adelaide, S.A., Australia, in 1989, and the Ph.D. degree from the University of Glasgow, Scotland, U.K., in 1993.

He worked at General Electric Corporate Research and Development, Schenectady, New York, before joining the University of Adelaide, in 1998. His research interests include permanent magnet and reluctance machines, renewable energy generation, and condition monitoring.

Gene S. Liew was born in Sabah, Malaysia, and received his B.Eng. and Ph.D. degrees in electrical and electronic engineering from the University of Adelaide, Australia, in 2003 and 2009. His research interests are in the analysis and design of axial and radial flux permanent magnet machines utilising amorphous magnetic material and soft magnetic composites.

Nesimi Ertugrul (M'95) received the B.Sc. degree in electrical engineering and the M.Sc. degree in electronic and communication engineering from the Istanbul Technical University, Turkey, in 1985 and 1989 respectively, and the Ph.D. degree from the University of Newcastle, Newcastle upon Tyne, U.K., in 1993.

He has been with the University of Adelaide since 1994, where he is an Associate Professor. His primary research topics include sensorless operation of switched machines, power electronics, renewable energy systems, fault-tolerant motor drives, power quality monitoring and condition monitoring. He is the author of a book, *LabVIEW for Electric Circuits, Machines, Drives, and Laboratories* (Prentice-Hall, 2002).